Facilitated Water Adsorption and Dissociation on Ni/Ni_3S_2 Nanoparticles Embedded in Porous S-doped Carbon Nanosheet Arrays for Enhanced Hydrogen Evolution

Yong Li,[†] Dipam M. Patel,[‡] Chui-Shan Tsang,[†] Renqin Zhang,[‡] Mengjie Liu,[†] Gyeong S. Hwang,*[,‡] and Lawrence Yoon Suk Lee*[,†,§]

[†] Department of Applied Biology and Chemical Technology and the State Key Laboratory of Chemical Biology and Drug Discovery, The Hong Kong Polytechnic University, Hung Hom, Kowloon, Hong Kong.

[‡] McKetta Department of Chemical Engineering, University of Texas, Austin, Texas, 78712, United States.

[§] Research Institute for Smart Energy, The Hong Kong Polytechnic University, Hung Hom, Kowloon, Hong Kong.

KEYWORDS: Ni/Ni_3S_2 hybrid nanoparticle; S-doped carbon nanosheet; electronic interaction; electrocatalytic hydrogen evolution

ABSTRACT

Three-dimensional carbon-based catalysts grown on a conductive substrate can offer superior electrocatalytic activities towards hydrogen evolution reaction (HER). We herein describe a novel method for *in situ* fabrication of hybrid Ni/Ni_3S_2 nanoparticles embedded in S-doped carbon nanosheet arrays (Ni/Ni_3S_2/SC NSAs) on carbon cloth. With the morphological merits of large surface area and high conductivity, Ni/Ni_3S_2/SC NSAs are demonstrated as an efficient and durable HER catalyst that requires merely 90 mV at a current density of 10 mA cm^{-2} with a small Tafel slope of 81 mV dec^{-1}. This excellent performance is ascribed to the formation of $Ni^{\delta+}$ and $S^{\delta-}$ species that promote the cleavage of H-OH bonds. First-principles calculations further reveal that the Ni surface near the Ni/Ni_3S_2 interface has a larger water adsorption energy (E_{ad}) and lower activation energy for water dissociation (E_a) than pure Ni and Ni_3S_2, which contribute to enhance HER performance. This work offers valuable insights into the designing of interface between transition metal-based catalysts and heteroatom-doped carbon materials.

1. INTRODUCTION

Water splitting is one of the most promising technologies for relieving the current heavy dependence on fossil fuels by realizing clean and sustainable production of hydrogen as a renewable energy carrier.[1,2] Hydrogen-based energy grid can provide a holistic solution not only for the escalating energy demands but also for the deepening environmental problems caused by the excessive use of fossil fuels. Till now, hydrogen production is mostly based on hydrocarbon reforming,[3] which is neither energy-efficient nor environmentally friendly. As an alternative to hydrogen reforming, electrochemical water splitting has great potential to become a sustainable pathway toward clean and efficient hydrogen production and storage. So far, Pt-based electrocatalysts have demonstrated the best performance in catalyzing hydrogen evolution reaction (HER) from water,[4,5] but their wide application is largely limited by the scarcity and high cost of Pt. Hence, it remains a great challenge to develop a cost-effective yet efficient and durable catalyst to promote the hydrogen production rate, which is vital for realizing a sustainable next generation energy system.

In the past two decades, carbon-based materials have attracted great interest in the energy conversion field owing to their desirable properties, such as tunable molecular structures, large surface area, and low cost.[6] Although pristine carbon usually shows poor catalytic activity toward HER, its catalytic performance can be largely improved by carefully designing and customizing the active sites. Non-metallic elements (*e.g.*, N, S, P, and B) have been doped into carbon network, such as N and S co-doped porous carbons and N doped graphene,[7–10] to effectively optimize the Gibbs free energy of H* absorption (ΔG_{H*}) by tailoring the electronic density state of carbon, thus improving HER activity. The majority of metal-free carbon-based catalysts, however, still suffer from insufficient catalytic activity that results in high overpotentials that often exceed 200 mV to attain a current density of 10 mA cm^{-2}.

Recently, the research on non-precious metal-based carbon composite catalysts has rapidly progressed with improvement in rational designs to construct nanocomposites of various metal phases (*e.g.*, metal alloys,[11] carbides,[12] phosphides,[13] nitrides,[14] and dichalcogenides[15]) and carbon materials, especially the heteroatom-doped ones, such as Co_9S_8 nanoparticles (NPs) embedded in N, S co-doped graphene-unzipped carbon nanotubes and P-doped carbon shelled Ni_2P NPs on graphene.[16,17] Ni_3S_2 has been recognized as a potential HER electrocatalyst that shows a better HER activity than other nickel chalcogenides (NiS and NiS_2).[18] It is known that the rich Ni-Ni and Ni-S bonds in Ni_3S_2 not merely increase the conductivity but also contribute to the optimized ΔG_{H^*} for efficient HER catalysis.[19] It has been reported that HER activity could be further enhanced by the formation of a Ni NP/Ni_3S_2 hybrid, with the metallic Ni providing abundant active sites and Ni_3S_2 facilitating the hydrogen desorption process.[20] Up to date, most of Ni_3S_2-based HER catalysts were estimated in alkaline media and thus the property of H_2O adsorption and dissociation is crucial for efficient hydrogen evolution. To facilitate H_2O adsorption and dissociation, the N_3S_2 is recommended to combine with another structure that has excellent adsorption ability. For example, Li's group modified Cu nanodots on Ni_3S_2 and their theoretical calculation results showed that the positive charged Cu could lower the water adsorption energy and accelerate the water dissociation.[21] Xu et al. also engineered heterogeneous interface on $Ni(OH)_2/Ni_3S_2$ to enhance the adsorption of OH^- group.[22] However, Ni_3S_2-based carbon composite catalysts are rarely reported and it is still unknown how the carbon composite affects the catalytic activity of Ni_3S_2. From a practical perspective, 3D carbon structure is more advantageous to the constructing of composite catalytic system for electrocatalytic applications. Compared with most 1D and 2D carbon materials (carbon nanotubes, graphene, and pyrolytic carbon nanosheets) that require immobilization on electrodes using Nafion or polytetrafluoroethylene (PTFE), a binder-

free 3D carbon structure offers a large surface area for electrolyte/electrode interface without compromising additional interface resistance or elongating the electron transfer path.[23] A simple, efficient, and cost-effective way for preparing a 3D structure of catalyst-embedded carbon composite is of great interest for various applications.

Herein, we present a novel 3D structure of hybrid Ni/Ni_3S_2 NPs embedded in S-doped carbon nanosheet arrays (abbreviated as Ni/Ni_3S_2/SC NSAs) prepared on a carbon cloth as a highly effective electrocatalyst for HER. We engaged thiolated oleic acid (S-OA) as the source of both sulfur and carbon to form the Ni/Ni_3S_2 hybrid NPs as well as a thin S-doped carbon layer. By a simple pyrolytic reaction of S-OA coated on the preformed $Ni(OH)_2$ NSA, ultrathin 3D Ni/Ni_3S_2/SC NSAs are directly grown on a conductive substrate, which can deliver remarkable HER performance as manifested by an overpotential of 90 mV at 10 mA cm^{-2}. The real active sites responsible for such a high activity are investigated by systematic structural modifications, *in situ* Raman spectroscopy, and density functional theory (DFT) calculations. Our work reveals the origin of the electrocatalytic activity of the TMD/carbon composite HER catalyst and offers useful insights into the designing of catalysts based on Ni and other transition metals.

2. EXPERIMENTAL SECTION

2.1. Reagents and materials. All reagents are of analytical grade and used without further purification. Oleic acid ($C_{18}H_{34}O_2$, OA, ≥99%), 1-hexanethiol ($C_6H_{14}S$, 95%), 2,2′-azobis(2-methylpropionitrile) ($C_8H_{12}N_4$, 98%),), nickel(II) nitrate hexahydrate ($NiNO_3{\cdot}6H_2O$, ≥98.5%), urea ($CO(CH)_2$, ≥98.5%), and ammonium fluoride (NH_4F, ≥98%) were purchased from Sigma-Aldrich, Inc. Nitric acid (HNO_3, 69 %) was obtained from BDH ProLab, VWR

International Pty Ltd. Carbon cloth was purchased from CeTech Co., Ltd. All solutions were prepared using Milli-Q water (15 MΩ cm/25 ℃).

2.2. Synthesis of sulfur-containing oleic acid. Thiolated oleic acid was synthesized according to a reported procedure with slight modifications.[24] In a typical synthesis, oleic acid (10 g, 35 mmol), 1-hexanethiol (45 mL, 0.42 mol), and 2,2′-azobis(2-methylpropoonitrile) (0.58 g, 3.5 mmol) were refluxed in a 100 mL round-bottomed flask at 70 °C for 8 h. After cooling down to room temperature, the yellowish solution was distilled to remove excess hexanethiol under ambient pressure. By-products, including dihexyl disulfide and 2,2,3,3-tetramethylsuccinonitrile, were removed by further distillation under reduced pressure at a maximum temperature of 150 °C until no dihexyl disulfide was detected by ^{1}H NMR spectroscopy. The oleic acid-derived thioether was obtained as a brown oil in 86 % yield.

2.3. Synthesis of $Ni(OH)_2$ nanosheet arrays. The synthetic procedure for the $Ni(OH)_2$ NSAs has been previously described in detail.[25] Briefly, $Ni(NO_3)_2{\cdot}6H_2O$ (3.93 mmol), urea (26.25 mmol), and NH_4F (10.5 mmol) were mixed in 70 mL water and stirred until completely dissolved and then transferred to a 100 mL Teflon-lined stainless-steel autoclave. A piece of carbon cloth (2 × 3 cm^2) was washed with HNO_3 (1.0 M), absolute ethanol, and DI-water in sequence in an ultrasonic bath for 10 min and placed in the autoclave. The autoclave was then heated at 100 ℃ for 8 h to yield $Ni(OH)_2$ NSAs as a precursor for the next step.

2.4. Synthesis of Ni/Ni_3S_2/SC nanosheet arrays. The carbon cloth containing as-obtained $Ni(OH)_2$ NSAs precursor was cut into small pieces (1 × 0.5 cm^2) for the subsequent electrochemical tests. The two-step synthetic route of Ni/Ni_3S_2/SC NSAs is depicted in Scheme 1. First, the S-OA solution was prepared by adding S-OA (200 mg) to hexane (1 mL) under magnetic stirring at room temperature. S-OA solution (50 μL) was added dropwise onto the prepared carbon

cloth containing $Ni(OH)_2$ NSAs (20 mg cm^{-2}), followed by heat treatment in a tube furnace in 500 ℃ for 30 min under Ar flow (40 sccm).

2.5. Synthesis of Ni/Ni_3S_2, Ni/C and Etching of S-doped C nanosheet arrays. The as-prepared $Ni(OH)_2$ NSAs was cut into small pieces (1 × 0.5 cm^2) and heated in a tube furnace at 400 ℃ for 2 h under a H_2 (10 %)/Ar flow (50 sccm) to synthesize metallic Ni on the carbon cloth. The generated Ni further reacted with Na_2S (3 mM, 15 mL) at 160 ℃ for 30 min by hydrothermal to synthesize Ni/Ni_3S_2 on the carbon cloth. To prepare Ni/C NSAs, oleic acid (OA, 10 μL) was dropped on $Ni(OH)_2$ NSAs, followed by heating at 500 ℃ for 30 min under Ar flow (40 sccm). The as-prepared Ni/Ni_3S_2/SC NSAs was immersed in HNO_3 (2.0 M) for 20 h. The etched sample was taken out from the HNO_3 solution, washed with Milli-Q water several times, and finally dried under N_2 flow.

2.6. Structural characterizations. The morphology and structure of the samples were characterized by scanning electron microscopy (SEM, Tescan VEGA3), transmission electron microscopy (TEM, JEOL-2100F) equipped with an X-ray energy dispersive spectrometer (EDX), powder X-ray diffraction (XRD，X'Pert PRO PHILIPS with Cu Ka radiation), and Raman scattering spectroscopy (Renishaw inVia Raman microscope). The chemical states of elements were determined by X-ray photoelectron spectroscopy (XPS, AC-2, Riken Keiki).

2.7. Electrochemical measurements. Electrochemical analyses were performed with a three-electrode system on an electrochemical workstation (CHI 760E, CH instruments Inc.) in KOH (1.0 M) aqueous solution. The as-prepared catalyst was used as a working electrode and a Hg/HgO electrode and a Pt plate were engaged as the reference and counter electrodes, respectively. Linear sweep voltammetric (LSV) curves were acquired by sweeping the potential from -0.6 to 0.2 V (*vs*. reversible hydrogen electrode, RHE) at a rate of 5 mV s^{-1} after stabilizing the working electrode

by scanning ten cycles between -0.4 and 0.1 V at a rate of 50 mV s^{-1}. Nyquist plots were obtained at the frequencies ranging from 100 KHz to 0.05 Hz at -0.22 V. The stability of the electrode was tested by monitoring the *i*-t curve for 12 hours at an applied potential of -0.22 V and comparing the LSV curves before and after the potentiostatic test. All potentials reported in this work are referenced to RHE, which is converted from the measured potential against the Hg/HgO electrode following **equation 1**:

$$E(V\ vs.RHE) = E(V\ vs.Hg/HgO) + 0.098 + 0.059 \times pH \qquad 1$$

All the LSV curves are *i*R-compensated.

2.8. Computational methods. All first-principles calculations based on density functional theory (DFT) were performed with the Vienna Ab Initio Simulation Package (VASP),[26] using the Projector Augmented-Wave (PAW) method with a cutoff energy of 400 eV.[27] Exchange-correlation energies were obtained using the Generalized Gradient Approximation method of Perdew, Burke, and Ernzerhof (PBE).[28] For geometric relaxations, the ionic positions were optimized until forces on all atoms that fell below 5×10^{-2} eV $Å^{-1}$, while electronic minimization for each step was terminated when the energy difference between steps fell below 10^{-5} eV. Calculations involving slab geometries contained a minimum of 10 Å spacing to prevent interactions with the periodic images. The Ni (111) and Ni_3S_2 (111) slab structures were constructed as 4 × 4 surface cells with 4 layers each. The Ni/Ni_3S_2 interface structure was constructed with 5 layers of Ni and 4 layers of Ni_3S_2 to minimize lattice mismatch. Reaction barriers were determined using the Nudged Elastic Band (NEB) method, with default settings, contained within the VASP Transition State Tools (VTST) package.[29] NEB images used the same force convergence criterion as relaxations. K-point sampling at Γ was used for reaction pathway

calculations. For electronic structure analysis, a 4 × 4 × 1 Γ-centered k-point mesh was used to ensure accuracy. Spin-polarization was accounted for in all calculations.

3. RESULTS AND DISCUSSION

Scheme 1 illustrates the synthetic procedure of hybrid Ni/Ni_3S_2 NPs embedded in S-doped carbon NSAs grown on a carbon cloth (Ni/Ni_3S_2/SC NSAs) using $Ni(OH)_2$ NSAs as a template. The reaction of $Ni(NO_3)_2$ with urea and NH_4F under hydrothermal conditions yields the vertically grown $Ni(OH)_2$ NSAs on a carbon cloth with a loading mass of *ca*. 5 mg cm^{-2} (**Figure S1**),[30] which are then wetted with pre-determined volume of S-OA solution. The subsequent heat treatment (500 °C) yields the S-doped carbon nanosheet arrays with Ni/Ni_3S_2 hybrid NPs embedded. The morphology of Ni/Ni_3S_2/SC NSAs revealed by SEM images (**Figure 1a**) appears to be very similar to that of $Ni(OH)_2$ NSAs. The high magnification and cross-sectional SEM images of Ni/Ni_3S_2/SC NSAs (**Figure 1b**) indicate that the thickness and size of the nanosheets remain unchanged during the S-OA coating/annealing process. TEM analysis, however, unveils that the entire nanosheet is composed of numerous small NPs (average d = 38 nm, **Figure 1c**). HR-TEM confirms the highly crystalline nature of these NPs (**Figure 1d**) with clear lattice spacings, which are also encased by thin carbon layers. There are two discernible domains identified, which display distinct lattice spacings of 0.176 and 0.204 nm ascribed to the (200) plane of metallic Ni and (202) plane of Ni_3S_2, respectively. In addition, a new lattice spacing of 0.189 nm, which is caused by the lattice overlapping, appears between the Ni and Ni_3S_2 phases, forming an active Ni/Ni_3S_2 interface. During the annealing process, the S-OA decomposes to produce highly reactive species, such as CH_3 and H_2S. The $Ni(OH)_2$ can be reduced by such species, *e.g.*, CH_3, to metallic Ni that may further react with H_2S to form Ni_3S_2 species.[31] Furthermore, H_2S also acts as a S donor to induce

S doping on the carbon nanosheets,[16] as confirmed by the subsequent X-ray photoelectron spectroscopic (XPS) measurements. The presence of Ni, S, and C atoms on the nanosheet is verified by the elemental mappings shown in **Figure S2**. For comparison, Ni NPs-embedded carbon NSAs (Ni/C NSAs) were also prepared by using OA directly (**Figure S3**).

Powder X-ray diffraction (XRD) was engaged to investigate the crystal structure of Ni/Ni_3S_2 NPs (**Figure 1e**). Two sets of peaks are identified; the peaks at 21.7°, 31.0°, 37.6°, 50.0°, and 55.1° can be indexed to the (101), (110), (003), (021), and (113) planes of Ni_3S_2 (JCPDS No. 44-1418), while those at 44.3°, 51.7°, and 76.3° are assigned to the (111), (200), and (220) planes of metallic Ni (JCPDS No. 04-0850), respectively, confirming the coexistence of Ni and Ni_3S_2 phases. Another broad peak observed at 25.5° can be ascribed to the graphitized carbon (JCPDS No. 75-2078).[32] Raman spectroscopy was engaged to gain further structural information of the carbon nanosheet (**Figure 1f**). Two major Raman peaks identified at 1,358 and 1,596 cm^{-1} are correlated to the D- and G-bands of sp^2-structured carbon, respectively, with a peak intensity ratio (I_D/I_G) of 0.71. This I_D/I_G value indicates that the carbon species in Ni/Ni_3S_2/SC NSAs is disordered graphitic carbon, most probably due to the S dopants.[33] To clarify the roles of S doping in the carbon layer and embedded NPs, bare Ni/Ni_3S_2 with no carbon coating was prepared on carbon cloths by reducing $Ni(OH)_2$ NSAs to Ni and then reacting it with Na_2S in a suitable condition (denoted as Ni/Ni_3S_2, **Figure S4**). Furthermore, Ni/Ni_3S_2/SC NSAs were immersed in 2 M HNO_3 for 20 hours in an effort to etch out Ni/Ni_3S_2 NPs (denoted as e-SC NSAs, **Figure S5**). Note that the TEM image of e-SC NSAs reveals that there are still a few small (<3 nm) residual NPs with a *d*-spacing of 0.204 nm that corresponds to the (202) plane of Ni_3S_2 phase, probably due to the low solubility of Ni_3S_2 in HNO_3. The atomic percentages of Ni, S, and C estimated by energy dispersive X-ray

analysis (EDX) indicate that S doping in SC is *ca*. 1.7 % and the weight ratio of Ni:Ni_3S_2 is close to 2:1 (**Figure S6**).

The composition and chemical states of Ni/Ni_3S_2/SC, Ni/Ni_3S_2, and e-SC were probed by X-ray photoelectron spectroscopy (XPS). As shown in **Figure 2a**, the fitted peak located at 856.2 eV in the Ni $2p_{3/2}$ spectrum of Ni/Ni_3S_2/SC is assigned to Ni^{2+}, while the one at a lower binding energy (852.9 eV) is ascribed to Ni^0.[34] In addition to the shakeup satellite peak at 860.9 eV, another peak (854.0 eV) lies between the binding energies of Ni^0 and Ni^{2+}, suggesting the presence of partially charged Ni species ($Ni^{\delta+}$, δ+ is a valence state between 0 and 2+).[20,34] Similar but much weaker peaks are observable in the spectrum of e-SC NSAs with the Ni^{2+} peak negatively shifted by 0.40 eV, which indicates that the Ni_3S_2 species are responsible for the partial electrons transfer. Also, a prominent increase in the Ni^{2+}/Ni^0 ratio suggests that the relative population of Ni_3S_2 over metallic Ni has increased which is in accordance with the TEM observations (**Figure S5**). Meanwhile, the $Ni^{\delta+}$ peak is absent in the spectrum of Ni/Ni_3S_2, which displays only Ni^0 and Ni^{2+} peaks that are negatively shifted by 0.5 eV. This suggests the intimate interaction between Ni/Ni_3S_2 and SC in the Ni/Ni_3S_2/SC NSAs.

The S 2p region of Ni/Ni_3S_2/SC (**Figure 2b**) shows the characteristic S^{2-} peak at 162.1 eV that can be assigned to Ni_3S_2. The two spin-orbit doublet peaks at 163.5 and 164.6 eV that corresponds to $2p_{3/2}$ and $2p_{1/2}$ of S-C species, respectively, provide clear evidence for the S doping in the carbon layer.[35] The existence of partially charged $S^{\delta-}$ species is also suggested by another peak at 162.7 eV that appears at a lower binding energy than that of S^0 (163.3 eV).[36] Upon acid etching, the S^{2-} and $S^{\delta-}$ peaks are dramatically reduced to appear as a tail in the S 2p spectrum of e-SC, indicating that most, but not all, Ni_3S_2 NPs have been removed. In addition, the S $2p_{3/2}$ and $2p_{1/2}$ peaks of S-C species are positively shifted by 0.15 and 0.3 eV, respectively, confirming that

S-doped C acts as an electron acceptor from the Ni_3S_2 phase. In the absence of S-doped carbon, the Ni/Ni_3S_2 exhibits only S $2p_{3/2}$ (162.0 eV) and S $2p_{1/2}$ (163.3 eV) peaks assigned to S^{2-} species, which are shifted to lower binding energies.[22] Such concomitant binding energy shifts in Ni/Ni_3S_2/SC imply a strong coupling effect that redistributes the electrons between Ni/Ni_3S_2 and SC, and hence induces the formation of $Ni^{\delta+}$ and $S^{\delta-}$ species.

The characteristic S-C peak, which arises from the S doping in carbon, is evident in the C 1s spectra of both Ni/Ni_3S_2/SC and e-SC NSAs (**Figure S7**). The binding energy of S-C peak is positively shifted by 0.2 eV in e-SC NSAs, a shift that agrees well with the observation in the S 2p spectra. The O 1s spectrum of Ni/Ni_3S_2/SC displays three peaks at 529.7, 531.7, and 533.1 eV (**Figure 2c**), which are assigned to Ni-O, $-OH^-$, and adsorbed H_2O (H_2O_{ad}), respectively.[22] The Ni-O signal is due to the inevitable partial oxidation of metallic Ni that is exposed to air. It is noteworthy that the relative peak area for OH^- and H_2O_{ad} peaks varies considerably in e-SC NSAs and Ni/Ni_3S_2. The $–OH^-$ peak in e-SC NSAs is largely reduced due to the removal of Ni/Ni_3S_2 NPs that provides $-OH^-$ adsorption sites, while the H_2O_{ad} peak in Ni/Ni_3S_2 becomes smaller than that in Ni/Ni_3S_2/SC, indicating that the S-doped carbon is beneficial to the enhancement of the water physisorption property.

The electrocatalytic HER activity of Ni/Ni_3S_2/SC NSAs was investigated and compared with those of Ni/Ni_3S_2, e-SC, Ni/C NSAs, commercial Pt/C, and bare carbon cloth (CC) using a standard three electrode system in 1.0 M KOH (**Figure 3a**). The linear sweep voltammograms (LSVs) show that the overpotentials required for CC, Ni/Ni_3S_2, and Ni/C NSAs to achieve a current density of 10 mA cm^{-2} are 514, 247, and 186 mV, respectively. The carbon layer formed by the pyrolysis of OA helps to preserve NSA morphology in Ni/C NSAs, which in turn allows a larger surface area than Ni/Ni_3S_2, leading to a better HER performance. The catalytic HER activity is further

improved when S-OA is used to form Ni/Ni_3S_2/SC NSAs as manifested by a much lower overpotential of 90 mV at 10 mA cm^{-2}. Ni/Ni_3S_2 NPs are believed to play a key role in promoting HER catalysis as suggested by the poorer performance of e-SC NSAs (311 mV). The corresponding Tafel plots given in **Figure 3b** shows that Ni/Ni_3S_2/SC NSAs exhibits the smallest Tafel slope of 81 mV dec^{-1} compared with e-SC NSAs (150 mV dec^{-1}), Ni/Ni_3S_2 (165 mV dec^{-1}), and Ni/C NSAs (110 mV dec^{-1}), indicating an enhanced HER kinetics on Ni/Ni_3S_2/SC NSAs. Based on the Tafel slope that falls between 40 and 120 mV dec^{-1}, a two-electron transfer process following the Volmer-Heyrovsky mechanism is suggested for Ni/Ni_3S_2/SC NSAs.[15]

Electrochemical impedance spectroscopy (EIS) was also employed to investigate the catalytic kinetics at the interface between the electrode and electrolyte, and the Nyquist plots were fitted by the simplified Randles cell (**Figure S8**). A similar trend is observed for charge-transfer resistance (R_{ct}); Ni/Ni_3S_2/SC NSAs show merely 3 Ω at -0.22 V (*vs*. RHE), followed by Ni/C NSAs (6 Ω), Ni/Ni_3S_2 (27 Ω), and e-SC NSAs (69 Ω). It is worth noting that the removal of hybrid Ni/Ni_3S_2 NPs has increased the R_{ct} of e-SC NSAs by more than twenty times, which indicates that the hybrid Ni/Ni_3S_2 NPs are crucial in the promoting of the electron transfer and catalytic kinetics.

It is well known that the number of active sites can largely affect the catalytic performance.[37] We thus estimated the electrochemical surface areas (ECSA) of samples by means of electrochemical double-layer capacitance (C_{dl}).[38,39] From a series of cyclic voltammograms (CVs) measured between 0.32 and 0.52 V (*vs*. RHE) at various scan rates from 5 to 100 mV s^{-1}, the C_{dl} values of 2.7, 7.4, 36.7, and 45.3 mF cm^{-2} were obtained from Ni/Ni_3S_2, Ni/C NSAs, e-SC NSAs, and Ni/Ni_3S_2/SC NSAs, respectively (**Figure 3c**). Relatively high C_{dl} values of e-SC and Ni/Ni_3S_2/SC NSAs suggest that the considerable enhancement in ECSA is certainly benefitted by the S-doped carbon matrix. Nevertheless, as indicated by the polarization curves, e-SC NSAs are

less catalytically active than Ni/C, implying that the HER activity should be attributed to the Ni-based species, rather than the larger carbon surface.

Long-term durability is another important criterion for evaluating an electrocatalyst. **Figure 3d** summarizes the chronoamperometric measurements conducted at -0.22 V (*vs*. RHE) in 1.0 M KOH. During the 12 hours of continuous electrolysis under a high overpotential, Ni/Ni_3S_2/SC NSAs maintain the initial current density with a minimal loss (3 %). In addition, the LSV after electrolysis is almost identical to the initial one (inset in **Figure 3d**), which again indicates the excellent stability of Ni/Ni_3S_2/SC NSAs. To further study their morphological changes and structural stability, the Ni/Ni_3S_2/SC NSAs were analyzed by XRD, SEM, and TEM after the continuous 1,000 cycles of potential sweep between -0.4 and 0.1 V. The results summarized in **Figure S9** show that the initial structure and morphology of Ni/Ni_3S_2/SC NSAs are well preserved, a result that can explain their stability and unchanged catalytic activity.

The HER of Ni/Ni_3S_2/SC NSAs under alkaline condition follows a Volmer-Heyrovsky mechanism, the first Volmer step ($H_2O + e^- \rightarrow H_{ad} + OH^-$) followed by Heyrovsky step ($H_2O + H_{ad} + e^- \rightarrow H_2 + OH^-$).[22] Water adsorption and the cleavage of H-OH bond in alkaline media are primarily responsible for the HER rate and are normally considered as rate-determining steps.[40,41] In the above reactions, the main product of each step contains the OH^- species, meaning that abundant sites for OH^- adsorption are beneficial to the dissociation of H-OH bonds and the generation of H_{ad} intermediates. Some recent works have demonstrated that partically charged species (such as $Ni^{\delta+}$, $Co^{\delta+}$, $P^{\delta-}$, and $S^{\delta-}$) play an improtant role in enhancing the catalytic HER activity.[42] To understand the effect of partially charged $Ni^{\delta+}$ and $S^{\delta-}$ species in Ni/Ni_3S_2/SC, the XPS spectra of Ni/Ni_3S_2/SC after HER catalysis were analyzed (**Figure S10**). The Ni $2p_{3/2}$ and S 2p spectra reveal the disappearance of $Ni^{\delta+}$ and $S^{\delta-}$ peaks along with the enhanced Ni^{2+} peak and a

new S-O peak, verifying that these species have been probably oxidized to amorphous $Ni(OH)_x/SO_x$.[34] These results indicate that the $Ni^{\delta+}$ and $S^{\delta-}$ species are sensitive to OH^- group as hydride acceptors so that the cleavage of HO-H bonds would be facilitated. To identify the active catalytic sites of Ni/Ni_3S_2/SC NSAs and thus gain a deeper insight into their highly promoted HER activity, *in situ* Raman spectroscopy was employed during LSV (**Figure 4a**). With the applied potentials over -0.176 V, a broad peak appears between 500 and 900 cm^{-1} and evolves as a peak at 814 cm^{-1}, which is assigned to the Ni-adsorbed H bond ($Ni-H_{ad}$) vibration.[43] More importantly, this peak disappears after the electrochemical test (**Figure S11**), confirming that the $Ni-H_{ad}$ bonds are formed as the intermediate species during HER. This agrees well with the electrochemical analyses that indicate the Ni sites are catalytically active sites in Ni/Ni_3S_2/SC NSAs.

We then performed DFT calculations to understand how HER, as well as water adsorption and dissociation, works on Ni/Ni_3S_2/SC surface. To simplify the calculation model, we only consider the close-packed (111) surfaces of Ni, Ni_3S_2, and Ni/Ni_3S_2 for direct comparison as both Ni and Ni_3S_2 phases are surrounded by SC (**Figure 4b** and **4c**). The calculated adsorption energies (E_{ad}) of water are 0.28 and 0.37 eV on the Ni(111) and Ni_3S_2(111) surfaces, respectively, which are in good agreement with previous DFT calculations (**Table 1**).[44,45] Here, E_{ad} is calculated by subtracting the total energy of the slab with the adsorbed water ($E_{H_2O/slab}$) from the sum of the energies of a gas phase water molecule (E_{H_2O}) and the slab model (E_{slab}), *i.e.*, $E_{ad} = E_{H_2O} + E_{slab} - E_{H_2O/slab}$. Our calculation predicts a substantial increase in E_{ad} to 0.62 eV on the Ni side of the Ni/Ni_3S_2 interface.

The dissociation of adsorbed water into adsorbed hydroxyl and hydrogen, *i.e.*, $H_2O^* \rightarrow HO^* + H^*$, is an exothermic reaction and the dissociation energies (ΔE_{diss}) are also summarized in Table 1. The predicted exothermicity is ΔE_{diss} = -0.35 eV on pure Ni(111) and slightly decreases to -0.30

eV on the Ni side of the Ni/Ni_3S_2 interface. On the other hand, the water dissociation reaction is predicted to be endothermic by ΔE_{diss} = 0.50 eV on pure Ni_3S_2(111), implying that it may rarely occur. The poor activity can be attributed, in part, to the relatively weak binding between H and S. We also calculated the activation energy of the water dissociation (E_a), which is 1.10 eV on pure Ni_3S_2(111) while decreasing to 0.89 eV on pure Ni(111) and further to 0.70 eV on Ni/Ni_3S_2(111). The relatively lower E_a and larger E_{ad} may suggest that the Ni surface near the Ni/Ni_3S_2 interface would be more active than the pure Ni counterpart. Moreover, our ongoing work shows that the water dissociation reaction may also involve multiple H_2O molecules that are connected by hydrogen bonds, as illustrated in **Figure S12**, where O in one H_2O molecule is favorably bound to a $Ni^{\delta+}$ site on the Ni_3S_2 side and H in another H_2O molecule interacts with a $Ni^{\delta-}$ site on the Ni side particularly when the Ni/Ni_3S_2 catalyst is charged negatively. Furthermore, the arrangement and dynamics of H_2O molecules near the Ni/Ni_3S_2 surface tend to affect the HER kinetics to a certain extent, while they can be noticeably altered by the presence of carbon shell as briefly demonstrated in **Figure S12**. The effects of catalyst charging and interfacial water dynamics will be presented elsewhere. Nonetheless, our theoretical work reported herein clearly demonstrates the enhancement of reactivity near the Ni/Ni_3S_2 interface that could be largely responsible for the higher activity of the Ni/Ni_3S_2/SC system as compared to the pure Ni system, although it would be hard to draw a definite conclusion based on the results of only a single facet and a single type of interface. Further investigations are underway to fully understand the complex relationship between surface modification and water dissociation kinetics (Volmer step).

This HER performance of Ni/Ni_3S_2/SC NSAs is close to that of Pt/C and surpasses the performances of most of the Ni_3S_2- and Ni-based electrocatalysts recently reported (**Table S1**). The overpotentials of those electrocatalysts are listed in **Figure 5**, showing that the Ni/Ni_3S_2/SC

NSAs exhibits a lower overpotential at 10 mA cm^{-2} than that of those reported ones. Based on the above observations, we attribute the superior HER activity of Ni/Ni_3S_2/SC NSAs to the following aspects: Firstly, the 3D quasi-vertical nanosheet arrays provide a large active surface area and easy pathway for the electron transfer from catalysts to electrode. Such vertical configuration is also advantageous in transporting reactants (H_2O) and products (H_2).[38] Secondly, the S-doped carbon and Ni/Ni_3S_2 NPs significantly improve the conductivity of Ni/Ni_3S_2/SC NSAs to facilitate the catalytic kinetics. Thirdly, the strong electronic interaction between thin SC and Ni/Ni_3S_2 positively charges the Ni in Ni/Ni_3S_2 NPs, making it easier to trap OH^- group and facilitating the dissociation of water. Lastly, the generated Ni/Ni_3S_2 interface facilitates water adsorption and dissociation and provides abundant active sites to enhance the HER activity.

4. CONCLUTIONS

In summary, hybrid Ni/Ni_3S_2 NPs embedded on S-doped carbon nanosheet were *in situ* grown on a carbon cloth as an efficient HER electrocatalyst in alkaline medium. High conductivity, large surface area, and binder-free nature of the Ni/Ni_3S_2/SC NSA electrode afforded an excellent HER activity with a low overpotential of 90 mV to reach a current density of 10 mA cm^{-2} and a small Tafel slope of 81 mV dec^{-1}, as well as excellent stability. The S-OA acted as both carbon and sulfur sources to produce the S-doped carbon nanosheet and active Ni/Ni_3S_2 interface, whose strong coupling interaction contributed to the excellent HER activity. Our first-principles calculations demonstrated that the adsorption and dissociation of water can be facilitated in the Ni/Ni_3S_2 interface system as compared with its pure counterparts, while the Ni sites near the Ni/Ni_3S_2 interface are proposed to be the active sites, as supported by the *in situ* Raman spectra that reveal the Ni-H_{ad} bonds during HER.

ASSOCIATED CONTENT

Supporting Information

This information is available free of charge on the ACS Publications website.

Supplementary data include SEM and TEM images and XRD patterns of Ni/Ni_3S_2/SC, Ni/Ni_3S_2, e-SC, Ni/C, and $Ni(OH)_2$ NSAs; EDX mapping and C 1s XPS spectrum of Ni/Ni_3S_2/SC; Ni $2p_{3/2}$ and S 2p spectra and Raman results of Ni/Ni_3S_2/SC before and after HER test; computational simulation of Ni/Ni_3S_2/SC in HER; summary of recent HER catalysts (Figures S1-S12 and Table S1).

AUTHOR INFORMATION

Corresponding Authors

*E-mails: gshwang@che.utexas.edu (G. S. Hwang)

lawrence.ys.lee@polyu.edu.hk (L. Y. S. Lee)

Author Contributions

Y. Li fabricated and characterized the catalysts and drafted the manuscript. D.M. Patel and Dr. R. Zhang performed DFT calculations and contributed to analyzing the results. D.M. Patel also participated in writing the manuscript. Dr. C.-S. Tsang synthesized the starting materials and M. Liu contributed to TEM analysis. Prof. G.S. Hwang guided the theoretical work and revised the manuscript. Prof. L.Y.S. Lee supervised this project and revised the manuscript.

Notes

The authors declare no competing financial interest.

Acknowledgments

This work was supported by the Innovation and Technology Commission of Hong Kong and Hong Kong Polytechnic University (1-BE0Y). G.S.H. gratefully acknowledges the support of the R.A. Welch Foundation (F-1535). We also thank Myungsuk Lee and Bohak Yoon in the Hwang group for sharing their simulation results on the arrangement and dynamics of water at the catalyst/water interface as well as the Texas Advanced Computing Center for use of the Stampede supercomputing system (OCI-1134872).

REFERENCES

(1) Dai, Z.; Geng, H.; Wang, J.; Luo, Y.; Li, B.; Zong, Y.; Yang, J.; Guo, Y.; Zheng, Y.; Wang, X.; Yan, Q. Hexagonal-Phase Cobalt Monophosphosulfide for Highly Efficient Overall Water Splitting. *ACS Nano* **2017**, *11*, 11031–11040.

(2) Li, J.; Xia, Z.; Zhou, X.; Qin, Y.; Ma, Y.; Qu, Y. Quaternary Pyrite-Structured Nickel/Cobalt Phosphosulfide Nanowires on Carbon Cloth as Efficient and Robust. *Nano Res.* **2017**, *10*, 814–825.

(3) Zeng, M.; Li, Y. Recent Advances in Heterogeneous Electrocatalysts for the Hydrogen Evolution Reaction. *J. Mater. Chem. A* **2015**, *3*, 14942–14962.

(4) Sheng, W.; Gasteiger, H. A.; Yang, S. Hydrogen Oxidation and Evolution Reaction Kinetics on Platinum : Acid vs Alkaline Electrolytes. *J. Electrochem. Soc.* **2010**, *157*, B1529–B1536.

(5) Nørskov, J. K.; Bligaard, T.; Logadottir, A.; Kitchin, J. R.; Chen, J. G.; Pandelov, S.; Stimming, U. Trends in the Exchange Current for Hydrogen Evolution. *J. Electrochem. Soc.* **2005**, *152*, J23–J26.

(6) Zhou, W.; Zhou, Y.; Yang, L.; Huang, J.; Ke, Y.; Zhou, K.; Li, L.; Chen, S. N-Doped Carbon-Coated Cobalt Nanorod Arrays Supported on a Titanium Mesh as Highly Active Electrocatalysts for the Hydrogen Evolution†. *J. Mater. Chem. A* **2015**, *3*, 1915–1919.

(7) Zhou, W.; Jia, J.; Lu, J.; Yang, L.; Hou, D.; Li, G.; Chen, S. Recent Developments of Carbon-Based Electrocatalysts for Hydrogen Evolution Reaction. *Nano Energy* **2016**, *28*, 29–43.

(8) Ito, Y.; Cong, W.; Fujita, T.; Tang, Z.; Chen, M. High Catalytic Activity of Nitrogen and Sulfur Co-Doped Nanoporous Graphene in the Hydrogen Evolution Reaction. *Angew. Chem. Int. Ed.* **2015**, *54*, 2131–2136.

(9) Liu, X.; Zhou, W.; Yang, L.; Li, L.; Zhang, Z.; Ke, Y.; Chen, S. Nitrogen and Sulfur Co-Doped Porous Carbon Derived from Human Hair as Highly Efficient Metal-Free Electrocatalysts for Hydrogen Evolution. *J. Mater. Chem. A* **2015**, *3*, 8840–8846.

(10) Shateesh, B.; Markad, G. B.; Haram, S. K. Nitrogen Doped Graphene Oxides as an Efficient Electrocatalyst for the Hydrogen Evolution Reaction; Composition Based Electrodics Investigation. *Electrochim. Acta* **2016**, *200*, 53–58.

(11) Deng, J.; Ren, P.; Deng, D.; Bao, X. Enhanced Electron Penetration through an Ultrathin Graphene Layer for Highly Efficient Catalysis of the Hydrogen Evolution Reaction. *Angew. Chem. Int. Ed.* **2015**, *54*, 2100–2104.

(12) Liu, Y.; Yu, G.; Li, G. D.; Sun, Y.; Asefa, T.; Chen, W.; Zou, X. Coupling Mo_2C with Nitrogen-Rich Nanocarbon Leads to Efficient Hydrogen-Evolution Electrocatalytic Sites. *Angew. Chem. Int. Ed.* **2015**, *54*, 10752–10757.

(13) Liu, Q.; Tian, J.; Cui, W.; Jiang, P.; Cheng, N.; Asiri, A. M.; Sun, X. Carbon Nanotubes Decorated with CoP Nanocrystals: A Highly Active Non-Noble-Metal Nanohybrid Electrocatalyst for Hydrogen Evolution. *Angew. Chem. Int. Ed.* **2014**, *53*, 6710–6714.

(14) Chen, W. F.; Sasaki, K.; Ma, C.; Frenkel, A. I.; Marinkovic, N.; Muckerman, J. T.; Zhu, Y.; Adzic, R. R. Hydrogen-Evolution Catalysts Based on Non-Noble Metal Nickel-Molybdenum Nitride Nanosheets. *Angew. Chem. Int. Ed.* **2012**, *51*, 6131–6135.

(15) Li, Y.; Wang, H.; Xie, L.; Liang, Y.; Hong, G.; Dai, H. MoS_2 Nanoparticles Grown on Graphene: An Advanced Catalyst for the Hydrogen Evolution Reaction. *J. Am. Chem. Soc.* **2011**, *133*, 7296–7299.

(16) Li, M.; Zhou, H.; Yang, W.; Chen, L.; Huang, Z.; Zhang, N.; Kuang, Y. Co_9S_8 Nanoparticles Embedded in a N,S Co-Doped Graphene-Unzipped Carbon Nanotube Composite as a High Performance Electrocatalyst for the Hydrogen Evolution Reaction†. *J. Mater. Chem. A* **2017**, *5*, 1014–1021.

(17) Miao, M.; Hou, R.; Liang, Z.; Qi, R.; He, T.; Yan, Y.; Qi, K.; Liu, H.; Feng, G.; Xia, B. Y. Chainmail Catalyst of Ultrathin P-Doped Carbon Shell-Encapsulated Nickel Phosphides on Graphene towards Robust and Efficient Hydrogen Generation†. *J. Mater. Chem. A* **2018**, *6*, 24107–24113.

(18) Jiang, N.; Tang, Q.; Sheng, M.; You, B.; Jiang, D.; Sun, Y. Nickel Sulfides for Electrocatalytic Hydrogen Evolution under Alkaline Conditions : A Case Study of Crystalline NiS, NiS_2, and Ni_3S_2 Nanoparticles. *Catal. Sci. Technol.* **2016**, *6*, 1077–1084.

(19) Feng, L.; Yu, G.; Wu, Y.; Li, G.; Li, H.; Sun, Y.; Asefa, T.; Chen, W.; Zou, X. High-Index Faceted Ni_3S_2 Nanosheet Arrays as Highly Active and Ultrastable Electrocatalysts for Water Splitting. *J. Am. Chem. Soc.* **2015**, *137*, 14023–14026.

(20) An, Y.; Huang, B.; Wang, Z.; Long, X.; Qiu, Y.; Hu, J.; Zhou, D.; Lin, H.; Yang, S. Constructing Three-Dimensional Porous Ni/Ni_3S_2 Nano-Interfaces for Hydrogen Evolution Electrocatalysis under Alkaline Conditions. *Dalt. Trans.* **2017**, *46*, 10700–10706.

(21) Feng, J.; Wu, J.; Tong, Y.; Li, G. Efficient Hydrogen Evolution on Cu Nanodots-Decorated Ni3S2 Nanotubes by Optimizing Atomic Hydrogen Adsorption and Adsorption. *J. Am. Chem. Soc.* **2018**, *140*, 610-617.

(22) Xu, Q.; Jiang, H.; Zhang, H.; Hu, Y.; Li, C. Heterogeneous Interface Engineered Atomic Configuration on Ultrathin $Ni(OH)_2$/Ni_3S_2 Nanoforests for Efficient Water Splitting. *Appl. Catal. B Environ.* **2019**, *242*, 60–66.

(23) Wen, W.; Chen, Y.; Wang, S.; Cao, M.; Yao, J.; Gu, Y. A 3D Electrode of Core@shell Branched Nanowire TiN@$Ni_{0.27}Co_{2.73}O_4$ Arrays for Enhanced Oxygen Evolution Reaction. *Appl. Mater. Today* **2018**, *12*, 276–282.

(24) Espinosa, L. M. D.; Gevers, A.; Woldt, B.; Graß, M.; Meier, M. A. R. Sulfur-Containing Fatty Acid-Based Plasticizers via Thiol–Ene Addition and Oxidation: Synthesis and Evaluation in PVC Formulations. *Green Chem.* **2014**, *16*, 1883–1896.

(25) Li, Y.; Hu, L.; Zheng, W.; Peng, X.; Liu, M.; Chu, P. K.; Lee, Y. S. L. Ni/Co-Based Nanosheet Arrays for Efficient Oxygen Evolution Reaction. *Nano Energy* **2018**, *52*, 360–368.

(26) Kresse, G.; Furthmüller, J. Efficient Iterative Schemes for Ab Initio Total-Energy Calculations Using a Plane-Wave Basis Set. *Phys. Rev. B* **1996**, *54*, 11169–11186.

(27) Blöchl, P. E. Projector Augmented-Wave Method. *Phys. Rev. B* **1994**, *50*, 17953–17979.

(28) Perdew, J. P.; Burke, K.; Ernzerhof, M. Generalized Gradient Approximation Made Simple. *Phys. Rev. Lett.* **1996**, *77*, 3865–3868.

(29) Henkelman, G.; Uberuaga, B. P.; Jónsson, H. Climbing Image Nudged Elastic Band Method for Finding Saddle Points and Minimum Energy Paths. *J. Chem. Phys.* **2000**, *113*, 9901–9904.

(30) Wang, H.; Wang, X. Growing Nickel Cobaltite Nanowires and Nanosheets on Carbon Cloth with Different Pseudocapacitive Performance. *ACS Appl. Mater. Interfaces* **2013**, *5*, 6255–6260

(31) Liu, Y.; Liu, Q.; Gu, J.; Kang, D.; Zhou, F.; Zhang, W.; Wu, Y.; Zhang, D. Highly Porous Graphitic Materials Prepared by Catalytic Graphitization. *Carbon N. Y.* **2013**, *64*, 132–140.

(32) Feng, Y.; Zhang, H.; Li, W.; Fang, L.; Wang, Y. Targeted Synthesis of Novel Hierarchical Sandwiched NiO/C Arrays as High-Efficiency Lithium Ion Batteries Anode. *J. Power Sources* **2016**, *301*, 78–86.

(33) Wopenka, B.; Xu, Y. C.; Zinner, E.; Amari, S. Murchison Presolar Carbon Grains of Different Density Fractions : A Raman Spectroscopic Perspective. *Geochim. Cosmochim. Acta* **2013**, *106*, 463–489.

(34) Liang, H.; Gandi, A. N.; Anjum, D. H.; Wang, X.; Schwingenschlögl, U.; Alshareef, H. N. Plasma-Assisted Synthesis of NiCoP for Efficient Overall Water Splitting. *Nano Lett.* **2016**, *16*, 7718–7725.

(35) El-sawy, A. M.; Mosa, I. M.; Su, D.; Guild, C. J.; Khalid, S.; Joesten, R.; Rusling, J. F.; Suib, S. L. Controlling the Active Sites of Sulfur-Doped Carbon Nanotube–Graphene Nanolobes for Highly Efficient Oxygen Evolution and Reduction Catalysis. *Adv. Energy Mater.* **2016**, *6*, 1501966.

(36) Meissner, D.; Benndorf, C.; Memming, R. Photocorrosion os Cadmium Sulfide: Analysis by Photoelectron Spectroscopy. *Appl. Surf. Sci.* **1987**, *27*, 423–436.

(37) Qu, K.; Zheng, Y.; Zhang, X.; Davey, K.; Dai, S.; Qiao, S. Z. Promotion of Electrocatalytic Hydrogen Evolution Reaction on Nitrogen-Doped Carbon Nanosheets with Secondary Heteroatoms. *ACS Nano* **2017**, *11*, 7293–7300.

(38) Zhang, Y.; Ouyang, B.; Xu, J.; Jia, G.; Chen, S.; Rawat, R. S.; Fan, H. J. Rapid Synthesis of Cobalt Nitride Nanowires: Highly Efficient and Low-Cost Catalysts for Oxygen Evolution. *Angew. Chem. Int. Ed.* **2016**, *55*, 8670–8674.

(39) Chen, P.; Xu, K.; Fang, Z.; Tong, Y.; Wu, J.; Lu, X.; Peng, X.; Ding, H. Metallic Co_4N Porous Nanowire Arrays Activated by Surface Oxidation as Electrocatalysts for the Oxygen Evolution Reaction. *Angew. Chem.* **2015**, *127*, 14923–14927.

(40) Subbaraman, R.; Tripkovic, D.; Chang, K. C.; Strmcnik, D.; Paulikas, A. P.; Hirunsit, P.; Chan, M.; Greeley, J.; Stamenkovic, V.; Markovic, N. M. Trends in Activity for the Water Electrolyser Reactions on 3d M(Ni,Co,Fe,Mn) Hydr(oxy)oxide Catalysts. *Nat. Mater.* **2012**, *11*, 550–557.

(41) Danilovic, N.; Subbaraman, R.; Strmcnik, D.; Chang, K. C.; Paulikas, A. P.; Stamenkovic, V. R.; Markovic, N. M. Enhancing the Alkaline Hydrogen Evolution Reaction Activity through the Bifunctionality of $Ni(OH)_2$/Metal Catalysts. *Angew. Chem. Int. Ed.* **2012**, *51*, 12495–12498.

(42) Li, J.; Jiang, L.; He, S.; Wei, L.; Zhou, R.; Zhang, J.; Yuan, D.; Jiang, S. P. Heterostructured $Ni(OH)_2/Ni_3S_2$ Supported on Ni Foam as Highly Efficient and Durable Bifunctional Electrodes for Overall Water Electrolysis. *Energy and Fuels* **2019**, *33*, 12052–12062.

(43) Qiu, Z.; Tai, C.; Niklasson, G. A.; Edvinsson, T. Direct Observation of Active Catalyst Surface Phases and the Effect of Dynamic Self-Optimization in NiFe-Layered Double Hydroxides for Alkaline Water Splitting. *Energy Environ. Sci.* **2019**, *12*, 572–581.

(44) Zhang, G.; Feng, Y.; Lu, W.; He, D.; Wang, C.; Li, Y.; Wang, X.; Cao, F. Enhanced Catalysis of Electrochemical Overall Water Splitting in Alkaline Media by Fe Doping in Ni_3S_2 Nanosheet Arrays. *ACS Catal.* **2018**, *8*, 5431–5441.

(45) Che, F.; Gray, J. T.; Ha, S.; McEwen, J. S. Catalytic Water Dehydrogenation and Formation on Nickel: Dual Path Mechanism in High Electric Fields. *J. Catal.* **2015**, *332*, 187–200.

List of Figures and Table

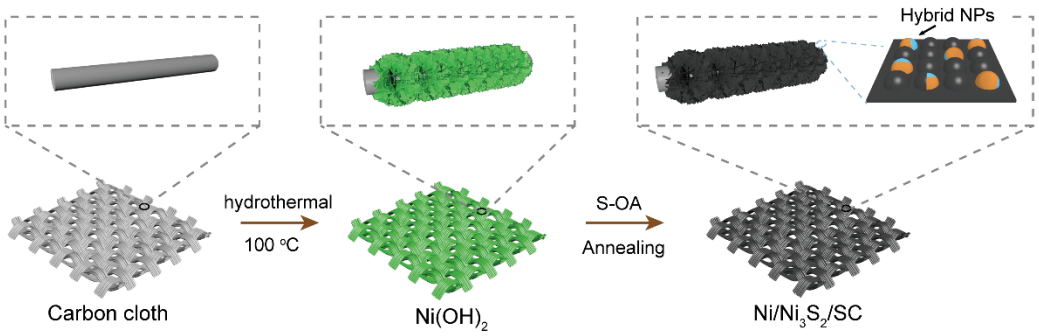

Scheme 1. Schematic illustration of the synthesis of $Ni/Ni_3S_2/SC$ NSAs on carbon cloth.

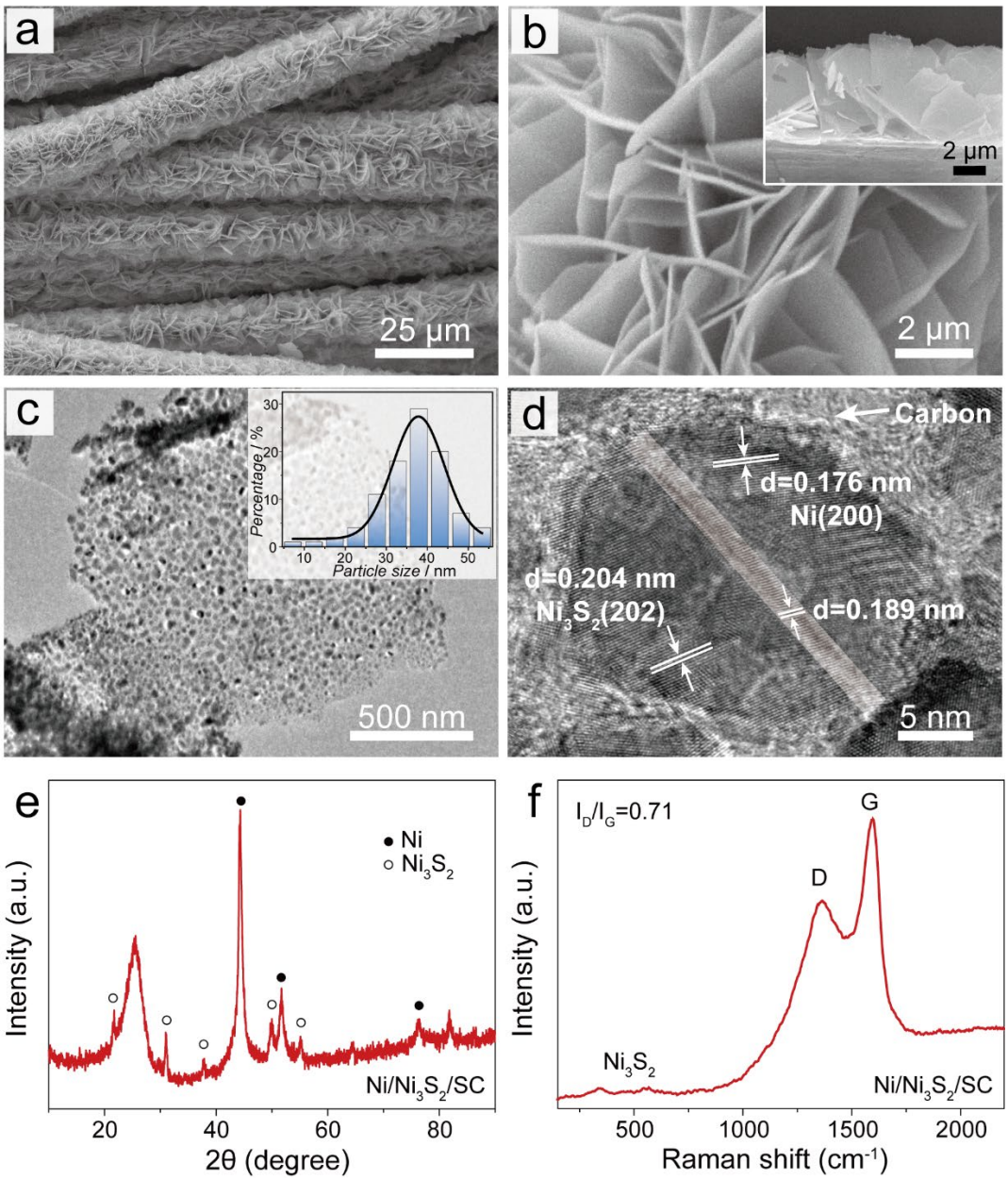

Figure 1. (a) Low- and (b) high-magnification SEM images, (c) low- and (d) high-resolution TEM images, (e) XRD pattern, and (f) Raman spectrum of $Ni/Ni_3S_2/SC$ NSAs. Insets in (b) and (c) are the cross-sectional view SEM and mid-resolution TEM images, respectively.

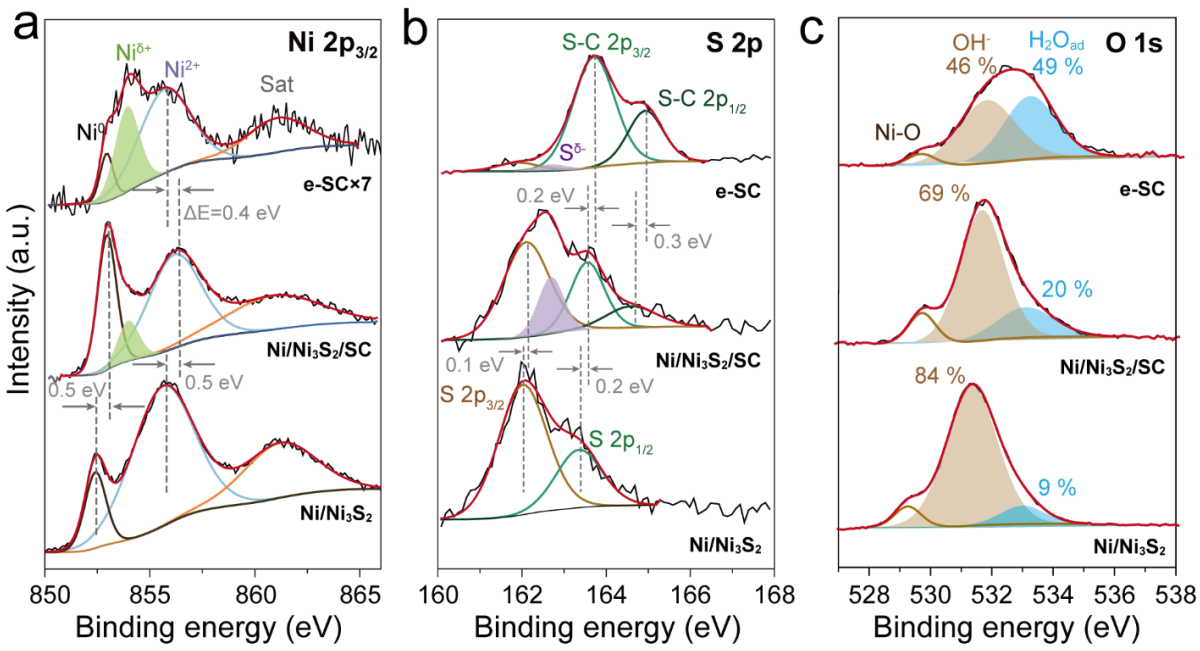

Figure 2. High-resolution XPS spectra of $Ni/Ni_3S_2/SC$, Ni/Ni_3S_2, and e-SC NSAs in (a) Ni $2p_{3/2}$, (b) S 2p, and (c) O 1s regions.

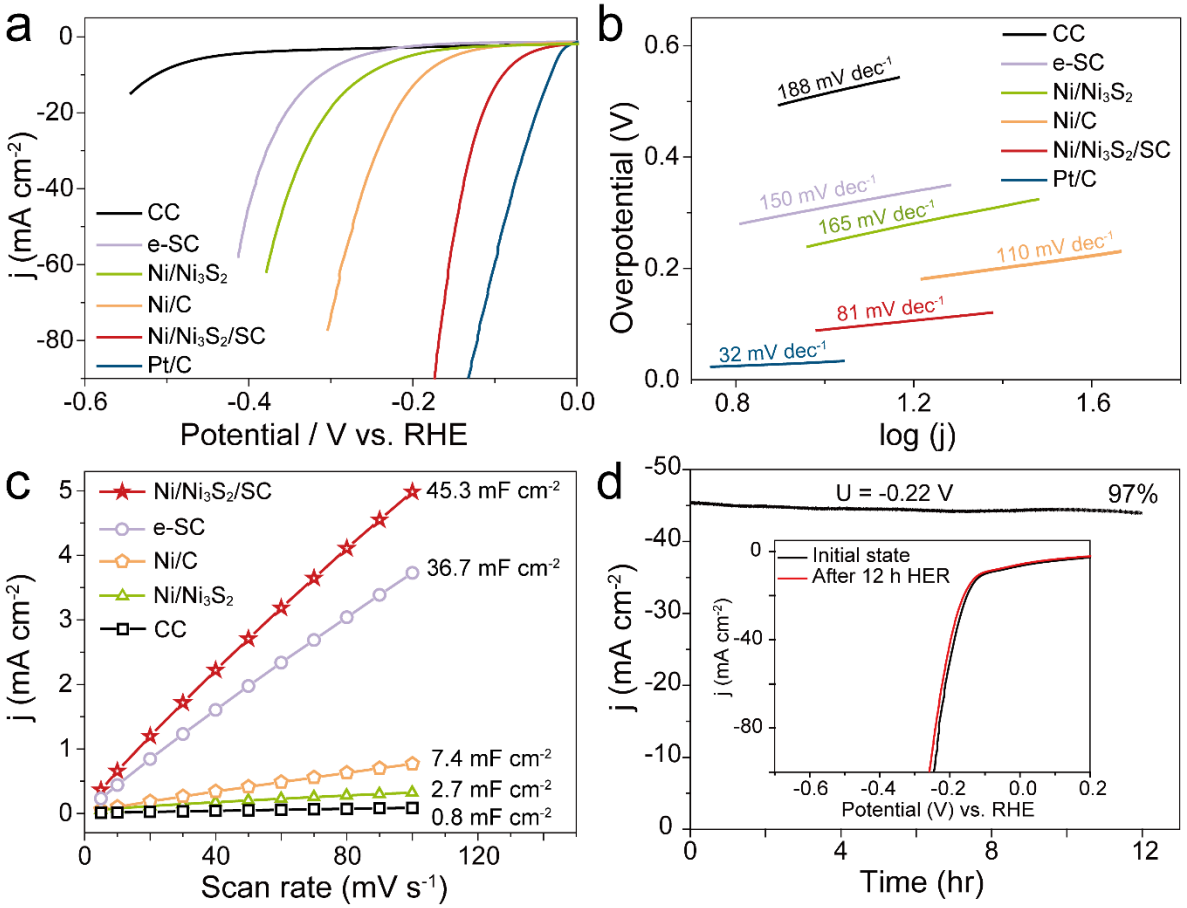

Figure 3. (a) Polarization curves and (b) Tafel plots of Ni/Ni_3S_2, Ni/C, Ni/Ni_3S_2/SC, and e-SC obtained from the electrocatalytic HER in 1.0 M KOH. (c) Capacitive currents plotted against the scan rates for Ni/Ni_3S_2, Ni/C, Ni/Ni_3S_2/SC, and e-SC. (d) Chronoamperometric plot of Ni/Ni_3S_2/SC at -0.22 V (*vs*. RHE). Inset is the polarization curves before and after continuous 12 h HER test. In (a)-(c), commercial Pt/C and carbon cloth (CC) were compared with the samples.

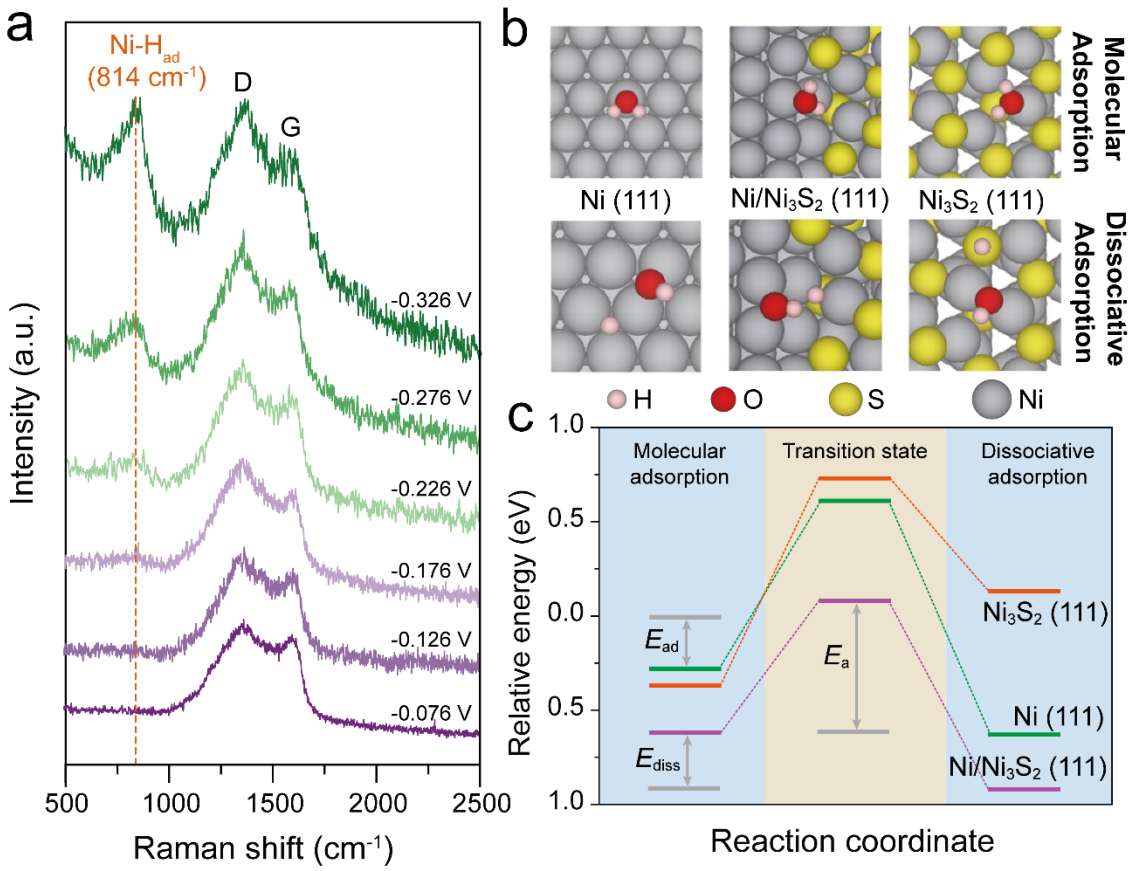

Figure 4. (a) In situ Raman spectra of Ni/Ni3S2/SC NSAs at various applied potentials (-0.076, -0.126, -0.176, -0.226, -0.276, and -0.326 V) in 1.0 M KOH. (b) Molecular (upper panels) and dissociative (lower panels) adsorption configurations of water on pure Ni(111), pure Ni3S2(111), and Ni/Ni3S2(111) surfaces. (c) Reaction energy diagrams for water adsorption (Ead) and dissociation (Ediss).

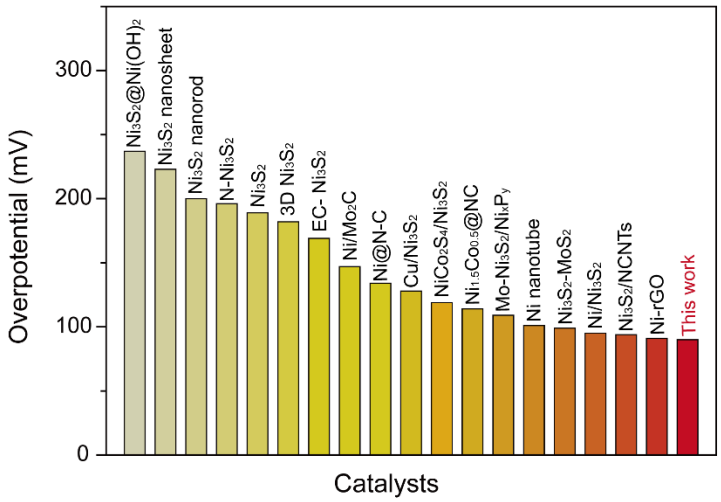

Figure 5. Summarized overpotentials of recent Ni-/Ni_3S_2-based electrocatalysts at 10 mA cm^{-2}.

Table 1. Single water adsorption energies (E_{ad}), energy barriers for dissociation of the adsorbed water (E_a), and energy changes in the water dissociation reaction (E_{diss}) on pure Ni (111), pure Ni_3S_2 (111), and Ni/Ni_3S_2 (111) surfaces. All values are given in eV units.

	E_{ad}	E_a	ΔE_{diss}
Ni (111)	0.28	0.89	-0.35
Ni_3S_2 (111)	0.37	1.10	0.50
Ni/Ni_3S_2 (111)	0.62	0.70	-0.30

TOC figure

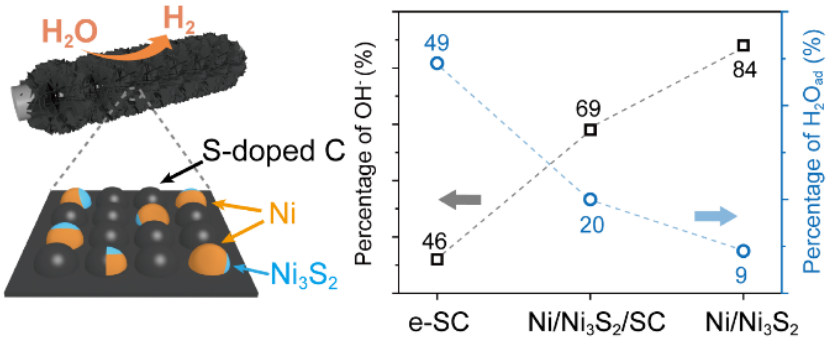
H2O
H2
S-doped C
Ni
Ni3S2
Percentage of OH- (%)
Percentage of H2Oad (%)
49
84
69
20
46
9
e-SC
Ni/Ni3S2/SC
Ni/Ni3S2